






Ultra-rapid electro-optic sampling of octave-spanning mid-infrared waveforms

ALEXANDER WEIGEL,^{1,2,3}  PHILIP JACOB,^{1,3}  DAVID GRÖTERS,³
THERESA BUBERL,^{1,3} MARINUS HUBER,^{1,3} MICHAEL
TRUBETSKOV,¹  JOACHIM HEBERLE,⁴ AND IOACHIM PUPEZA^{1,3,*} 

¹Max-Planck-Institut für Quantenoptik, Hans-Kopfermann-Str. 1, 85748 Garching, Germany

²Center for Molecular Fingerprinting, Molekuláris- Ujjenyomat Kutató Közhasznú Nonprofit Kft., 1093 Budapest, Czuczor utca 2-10, Hungary

³Fakultät für Physik, Ludwig-Maximilians-Universität München, Am Coulombwall 1, 85748 Garching, Germany

⁴Department of Physics, Experimental Molecular Biophysics, Freie Universität Berlin, Arnimallee 14, 14195 Berlin, Germany

*ioachim.pupeza@mpq.mpg.de

Abstract: We demonstrate ultra-rapid electro-optic sampling (EOS) of octave-spanning mid-infrared pulses centered at 9 μm , implemented by mechanically scanning a mirror with a sonotrode resonating at 19 kHz (forward and backward acquisition at 38 kHz). The instrument records the infrared waveform with a spectral intensity dynamic range of 1.6×10^5 for a single scan over a 1.6-ps delay range, acquired within 26 μs . The purely reflective nature of the delay scanning technique is compatible with broad optical bandwidths, short pulse durations (16 fs, centered at 1030 nm) and high average powers (Watt-level). Interferometric tracking of the sonotrode motion in combination with a predictor-corrector algorithm allows for delay-axis determination with down to single-digit attosecond precision. Ultra-rapid mid-infrared EOS will advance applications such as molecular fingerprinting of static samples as well as tracking of biological processes and chemical reactions and is likely to find new fields of application such as infrared-spectroscopic flow cytometry.

© 2021 Optical Society of America under the terms of the [OSA Open Access Publishing Agreement](#)

1. Introduction

In the last few decades, electro-optic sampling (EOS) has evolved as a standard technique to map the electric field of temporally coherent light with a short gate pulse, thereby overcoming limitations of common detectors that measure time-integrated light intensity [1–5]. The square-root relation between electric field and light intensity gives EOS a principal advantage in sensitivity and measurement dynamic range compared to conventional detection schemes [6]. EOS has proven particularly useful for the detection of mid-infrared (mid-IR) waveforms because it detects the mid-IR field-induced gate pulse modulation with low-noise near-infrared detectors rather than relying on relatively noisy mid-infrared detectors. Even more, in combination with ultrashort driving pulses the direct access to the time-dependent electric field allows for the intense excitation of a sample to be separated from the potentially weak molecular response. Combining all these advantages, it has been shown that field-resolved detection with EOS can reach sensitivities and specificities beyond the capabilities of currently employed Fourier transform spectroscopy (FTS) in the infrared molecular fingerprint region [2,3,6].

One of the shortcomings limiting the sensitivity and reproducibility not only in EOS, but also in other detection schemes employing scanned delays like, *e.g.*, FTS [7], femtosecond pump-probe and multi-dimensional spectroscopies [8], is the speed of the optical delay scan. Conventionally, scans are realized by moving a retroreflector with a motorized stage. While this approach is flexible regarding spectral bandwidth, laser pulse duration, precision and delay range,

the acquisition rate is slow, typically in the Hz range. During a slow scan, the recorded traces accumulate low-frequency noise, *e.g.*, from the dominant sub-kHz noise components of typical laser sources [9] or from acoustic vibrations and mechanical drifts [3,10,11]. Acquiring full delay scans at a multi-kHz rate circumvents this limitation by ‘freezing’ low-frequency noise contributions within the duration of a single scan.

In addition to the mitigation of low-frequency noise, ultra-rapid scanning at multi-kHz rates is necessary for real-time investigation of sub-millisecond chemical processes like protein refolding [12,13], combustion [14], solvent mixing [15] or irreversible protein reactions [16], and has applications in hyperspectral imaging [17,18] and high-throughput spectral flow cytometry [19].

Several approaches to multi-kHz optical scanning over picosecond delay ranges have been explored in the past. Acousto-optic modulation of the output of a mode-locked oscillator has been shown to yield highly reproducible 6-ps-long delay scans at ~ 35 kHz [20], and has been applied to linear interferometry [20], EOS detection of THz waveforms [21] and hyperspectral Raman imaging [18]. The main restrictions of acousto-optic modulators are their limited spectral bandwidth, low diffraction efficiency and incompatibility with pulses shorter than a few tens of femtoseconds. Another recent approach directly synchronizes and modulates the repetition frequencies of two separate laser oscillators [22,23]. While being highly versatile, such electronically controlled optical sampling (ECOPS) relies on involved locking schemes, with the achievable timing jitter still being on the order of several femtoseconds [24–26], falling short of the requirements of many ultrafast experiments.

Purely mechanical techniques based on the fast movement of a mirror are comparatively simple and can support spectrally broadband and ultrashort pulses. Initial approaches achieved fast scanning by rotation of a tilted mirror [14] or mirror array [27]. More recently, angular movement of a galvanometric scanner [15] or a polygon scanner [28] in 4f imaging geometries, also in combination with a dispersive element, were used for Fourier transform spectroscopy [28] and coherent anti-stokes Raman spectroscopy [15,19], with scan rates greater than 20 kHz. The most direct analogon to classical delay scanning is the linear forward and backward motion of a mirror, which has been realized by amplifying the resonant movement of a piezoelectric transducer oscillating at 19 kHz with a sonotrode to the multi-hundred micrometer scale [12]. This approach has been applied to time-resolved infrared FTS of proteins with an incoherent source [12].

In this work we employ the ultra-rapid motion of a mirror attached to a sonotrode to vary the delay of 16-fs near-infrared gate pulses used to record EOS traces of octave-spanning mid-IR pulses at a rate of 38,000 scans per second. The combination of bright, spatially and temporally coherent laser light with EOS detection affords a spectral intensity dynamic range of 1.6×10^5 in a single scan. Via interferometric measurement using a continuous-wave pilot laser, we track the free-oscillating sonotrode movement and retrieve the delay axis for each scan with attosecond precision. This reproducibility permits averaging for several seconds without signal deterioration. Sub-100- μ s referencing in EOS of mid-IR waveforms opens the door to new levels of sensitivity and specificity in biomedical sensing [3], as well as to new applications such as high-throughput mid-IR flow cytometry.

2. Experimental details

The experimental ultra-rapid scanning EOS setup is depicted schematically in Fig. 1(a). An Yb:YAG thin-disc oscillator provides 100 W of 260-fs pulses centered at 1030 nm, at a repetition rate of 28 MHz [29]. The output is further compressed in a two-stage multi-pass Herriott cell compressor [30], yielding 16-fs pulses with an average power of 60 W.

The gate beam for EOS is split off from the compressed beam by a Fresnel reflection at a fused silica window (FS). A combination of dispersive mirrors (DM) and fused silica plates (FS) ensures compression of the 300-mW gate pulses at the EOS crystal position.

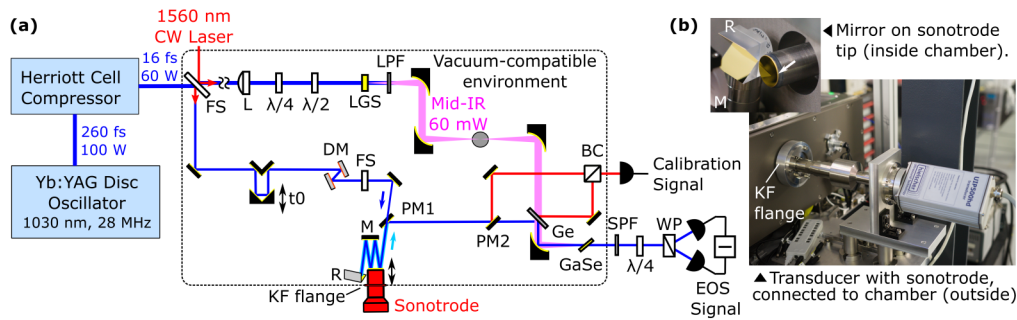


Fig. 1. (a) Experimental setup. The pulses from an Yb:YAG disc oscillator with subsequent Herriott cell multi-pass compressor (16 fs, 60 W, 28 MHz), are focused (lens L) into an LGS crystal for mid-IR generation. Quarter- ($\lambda/4$) and half-wave ($\lambda/2$) plates adjust the input polarization. A long-pass filter (LPF) removes the fundamental beam after the crystal. Fresnel reflection of the input beam at a fused silica plate (FS) generates the EOS gate beam, which is compressed with dispersive mirrors (DM) and a fused silica (FS) plate. It is sent over the sonotrode using mirror M, retro-reflector R, and picked up by mirror PM1 to be recombined with the mid-IR beam at a Germanium plate (Ge), after which both are focused into the GaSe crystal for EOS. The EOS signal is detected with an ellipsometric detection consisting of a short pass filter (SPF), a quarter-wave plate ($\lambda/4$), a Wollaston prism (WP) and a balanced detector. A delay calibration signal is generated interferometrically by coupling a 1550-nm CW pilot laser into the two arms via the FS plate, separated again by Ge and the pickup mirror PM2, and re-combined at BC. (b) Pictures of the sonotrode assembly, attached with a vacuum-compatible flange to the experimental chamber.

Forward/backward scanning at 38 kHz is achieved by exciting a sonotrode (Hielscher, BS4d22) to a 60- μm (peak-to-peak) resonant oscillation at 19 kHz *via* a combination of ultrasonic transducer (Hielscher, UIP500hd) and booster (Hielscher, BS2-3.0). Using mirror M and retroreflector R the gate beam is reflected four times at a mirror glued to the tip of the sonotrode (see appendix A), leading to a total delay range of 1.6 ps. The beam is then picked up with mirror PM1 and combined with the mid-IR beam *via* a 2-mm thick germanium plate.

The mid-IR beam is generated by focusing the remaining part of the 60-W, 16-fs pulses with an $f = 600$ mm lens (L) into a 1-mm thick LiGaS₂ (LGS) crystal [31]. Intra-pulse difference frequency generation (IPDFG) produces 60 mW of few-cycle mid-IR pulses, which contain spectral components in the range ~ 6 -12 μm (see results section for temporal and spectral characteristics). Quarter- and half-wave plates are used to optimize the conversion conditions. After the LGS crystal, a long-pass filter (LPF) removes the remaining fundamental part of the beam and transmits the mid-IR pulses.

After combination at Ge, the mid-IR and gate beams are collinearly focused into a 100- μm thick GaSe crystal to generate the delay-dependent EOS signal. For the EOS crystal thickness used here, the measured EOS waveform closely resembles the actual electric field [3,31]. After the crystal, the sampling beam passes through a 930-nm short-pass filter (SPF) [11], before the mid-IR field induced polarization rotation is detected in a standard ellipsometry setup [32], consisting of a quarter wave plate ($\lambda/4$), a Wollaston prism (WP) and an amplified balanced detector with 100 MHz bandwidth (Femto HBPR-100M-60K-IN). Note that we do not use lock-in detection in this experiment.

The current experiment was carried out under ambient-air conditions, but the sonotrode setup is also compatible with measurements under vacuum conditions. The sonotrode is fed into the experimental chamber *via* a vacuum-compatible flange (see Fig. 1(b)), positioned at a node of

the longitudinal sonotrode oscillation, so that the chamber can be evacuated while the sonotrode moves.

The motion of the freely oscillating sonotrode is tracked interferometrically with a 1550-nm continuous-wave (CW) beam (amplified output of a SmarAct Picoscale device) that is coupled via FS into the gate and mid-IR generating arms of the setup. Due to insufficient transmission, the calibration CW beam needed to bypass the Ge plate and is recombined at beam combiner BC instead. The resulting delay-dependent interferometric signal is detected with an amplified photodiode (Thorlabs PDA05CF2).

Both EOS and delay calibration signals are recorded simultaneously with a high-speed data acquisition card (Gage Compuscope Razor Express 16), with the acquisition rate synchronized to four times the laser repetition rate (112 MHz) to ensure that the sampling of the calibration interferogram fulfils the Nyquist criterion. We collected EOS and calibration signals continuously over a duration of 9.5 s, corresponding to $> 10^9$ data points per acquisition channel.

The interferogram recorded as the delay calibration signal is the linear autocorrelation of the CW laser and comprises the delay information with sub-wavelength precision. We use a predictor-corrector algorithm to extract the delay axis (see appendix B for details). The algorithm reliably converges for our data over hundreds of thousands of scans without any apparent outliers. It is robust to the input parameters, and – as we show in the results and discussion section – affords EOS waveforms with timing reproducibility in the attosecond range. The algorithm is applicable to any Mach-Zehnder-type scanning experiment with interferometric delay tracking. Because it naturally progresses from one data point to the next, it is also suitable for implementation of real-time data processing of the incoming data stream.

The acquired EOS signal was baseline-corrected with a Fourier high-pass filter. In addition, we corrected the delay axis for each scan with a sub-femtosecond shift to optimally overlay all waveforms. This step also corrects for jitter and drifts from differences of the optical paths of the delay calibration and EOS signals due to the fact that the CW bypasses the Ge plate (see Fig. 1(a)). Finally, all EOS scans were interpolated to a common delay axis.

3. Results

A single EOS trace, recorded with the ultra-rapid scanning setup during one half-cycle of the mirror oscillation with an acquisition time of 26 μ s, is shown in Fig. 2(a) (black, overlaid by the pink average trace). Each data point of the trace was acquired with a single laser shot. In order to illustrate the dynamic range and the effect of averaging, we start acquisition 1.3 ps before the pulse, where the signal of the single pulse reaches the baseline noise. The bottom panel shows the EOS signal for such a measurement recorded with a blocked infrared beam to demonstrate the detection noise. We define the time-domain electric field dynamic range (DR) as the maximum EOS signal of the time-domain trace divided by the root mean square (RMS) of the detection noise, and determine a value of 150 for the single-shot measurement. The waveform displayed in the top panel corresponds to a mid-infrared pulse of 115 fs duration having only 4 electric-field cycles within the full width of the half intensity maximum (FWHM).

The arithmetic mean of 365,800 single scans, including measurements with both forward and backward motions of the sonotrode, is shown in pink. The total acquisition time was approximately 9.5 s. The trace reproduces both the shape and the amplitude of the signal recorded in a single measurement, rendering the two traces in the top panel hardly distinguishable. This consistency demonstrates that the delay axis retrieval is highly reproducible over hundreds of thousands of traces for both forward and backward motions, because any major jitter would lead to a decrease in signal amplitude upon averaging. Furthermore, the observed behavior evidences that the mid-IR waveform generated by IPDFG is stable over the measurement time with a highly stable carrier-envelope phase [3,31,33,34].

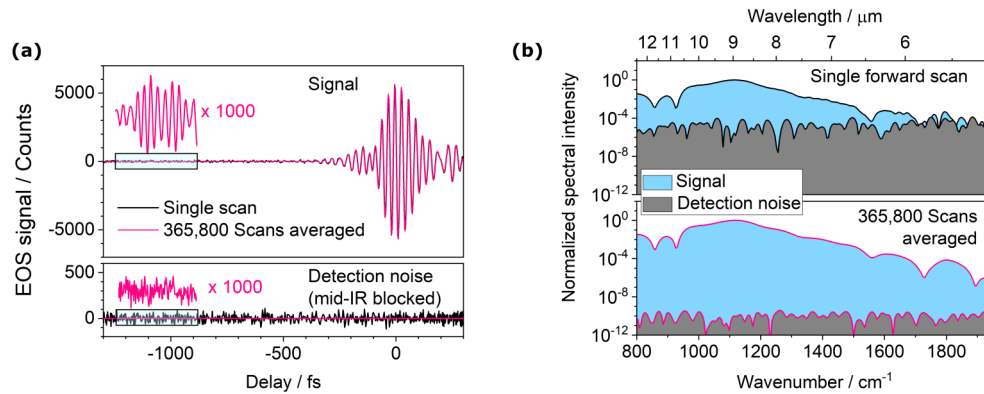


Fig. 2. (a) Electro-optic sampling (EOS) traces of a mid-IR pulse generated by intra-pulse difference frequency generation: Single forward scan (black), and all forward and backward scans over 9.5 s acquisition time averaged (pink), and comparison to the detection noise with the mid-IR blocked. (b) Intensity spectra obtained by Fourier transformation of (a).

A 1000-fold magnified section of the signal around -1000 fs delay demonstrates the sensitivity reached upon averaging by revealing the clean oscillations of the electric field building up already before the main pulse. The average baseline in the bottom panel is still featureless over the full delay range. In agreement with statistical noise behavior, the time-domain electric field DR increases upon averaging from 150 to 8×10^4 , approximately with the square root of the number of averaged traces.

Intensity spectra obtained by Fourier transformation of the traces in Fig. 2(a) are shown in Fig. 2(b). The mid-IR spectrum has a maximum at 1100 cm^{-1} ($9 \mu\text{m}$) and resembles in shape previously published results obtained with standard scanning EOS of infrared pulses generated by similar systems [3,31]. The detectable spectral components cover more than an octave of bandwidth, at least from 800 to 1900 cm^{-1} . We assign the dips above 1500 cm^{-1} to water vapor absorption, and the ones around 900 cm^{-1} to phase matching in the EOS crystal and absorption by the optical coatings.

The spectral intensity DR, defined by the maximum spectral intensity signal divided by the intensity RMS noise of the baseline, reaches a value of 1.6×10^5 already for a single scan and increases approximately linearly with averaging to 4×10^{10} for 365,800 scans, acquired in 9.5 s.

In order to further quantify the temporal stability of the measured EOS traces we investigate the zero crossing positions of the waveforms, obtained from linear fits to ca. 7-fs long segments as shown in red in the top panel of Fig. 3(a). The bottom panel of Fig. 3(a) shows the standard deviation of the zero crossings, σ_{zc} , over nine consecutive scans, and its behavior upon averaging. For single forward scans with $23 \mu\text{s}$ acquisition time, the trace-to-trace σ_{zc} lies in the range 23-34 as within the intensity FWHM of the pulse (yellow shaded area). The precision of the zero-crossing position is mainly limited by the time-domain electric field DR of the evaluated EOS signal, and σ_{zc} increases with decreasing signal amplitude towards the wings of the pulse. We therefore regard σ_{zc} as an upper boundary to the actual timing jitter of the mid-IR waveform. Accordingly, averaging packets of 256 consecutive forward and backward traces (including both forward and backward traces) reduces σ_{zc} to 1-2 as within the intensity FWHM of the pulse (blue). Averaging more traces does not improve σ_{zc} further. Instead, the shape of the σ_{zc} curve changes as shown for 38,000 scans averaged (dashed), indicating slow drifts and distortions of the waveform.

The dependence of σ_{zc} on the number of traces averaged is studied in Fig. 3(b) for the zero crossing marked by the dotted black line in Fig. 3(a). For up to 256 averaged traces (7 ms

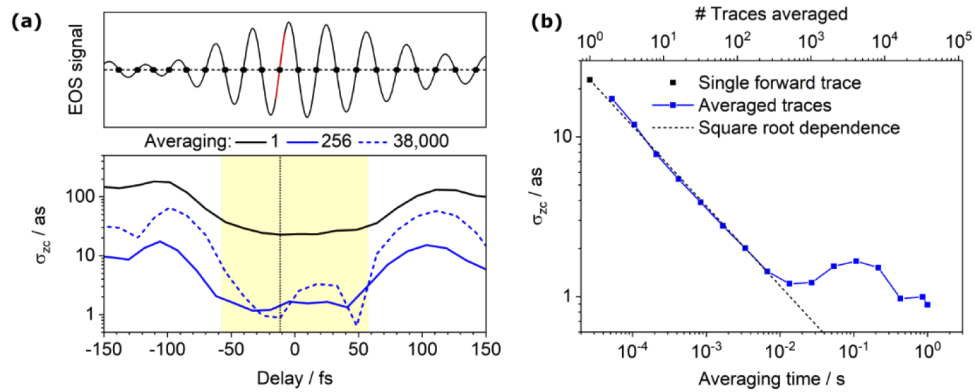


Fig. 3. (a) Top: the timing jitter of the zero crossings (black dots) of the EOS waveform was evaluated by a linear fit (red). Bottom: standard deviations of the zero crossing positions σ_{zc} , for different numbers of traces averaged. The yellow shaded area marks the section within the pulse intensity full width of half maximum. (b) Dependence of σ_{zc} on averaging time for the zero crossing marked by the dotted line in (a). The dashed line shows the square-root dependence expected for statistical measurement noise.

acquisition time) σ_{zc} decreases linearly with the number of averages, showing the dominance of statistical noise contributions. With further averaging, σ_{zc} deviates from the square-root dependence and does not decrease much further, marking the onset of drifts (on the time scale of the measurement). The sub-100-Hz regime is characteristic for acoustic vibrations and mechanical drifts, and we attribute the observed changes that prevent us from reaching the zeptosecond timing jitter regime to two main effects: (i) infrared waveform distortions induced by low-frequency laser noise; (ii) drifts and mechanical vibrations of the EOS detection setup that are not fully captured by the current delay axis calibration. The main source of delay noise is likely to be linked to the slightly different paths of the EOS and delay calibration beams (Fig. 1(a)). While we correct for systematic drifts of the full delay axis by shifting the signal during data processing (see appendix), a fully common interferometer arrangement can be expected to reduce slow delay variations further and would eventually enable sub-attosecond timing precision for the averaged waveforms.

The reproducibility of subsequent EOS waveforms paves the way for new referencing techniques. Having deduced in the previous paragraphs that the waveform changes from one EOS acquisition to the next are dominated by the signal noise, one can expect that subtracting two subsequent EOS scans yields an essentially flat line with a baseline noise increased by $2^{1/2}$. Figure 4(a), top, shows a single such difference trace, with the details for the difference formation depicted in Fig. 4(b): forward and backward scans of a single sonotrode cycle (blue and yellow shaded) were averaged, and the corresponding average scan from the next sonotrode cycle was subtracted (see appendix C for details). As expected, the difference formation cancels the signal almost completely, with only slight residual structure around the position of the main pulse. The residual signal may reflect multi-kHz fluctuations of the mid-IR pulses, but could also contain contributions from data processing, *e.g.*, from interpolation or numerical errors. Averaging the two scans of a sonotrode cycle should exactly compensate the $2^{1/2}$ noise increase by difference formation. Accordingly, the RMS noise of the single difference trace in Fig. 4(a) (8.5×10^{-3}) is close to the baseline noise of the single forward EOS trace in Fig. 2(a) (6.7×10^{-3}).

The analogon to a slow, multi-second long experiment with fast detection is simulated in the middle panel of Fig. 4(a) by averaging traces over a duration of 4.75 s before subtraction (see also 4b), corresponding to referencing at a rate of ~ 0.1 Hz. Note that in a conventional delay

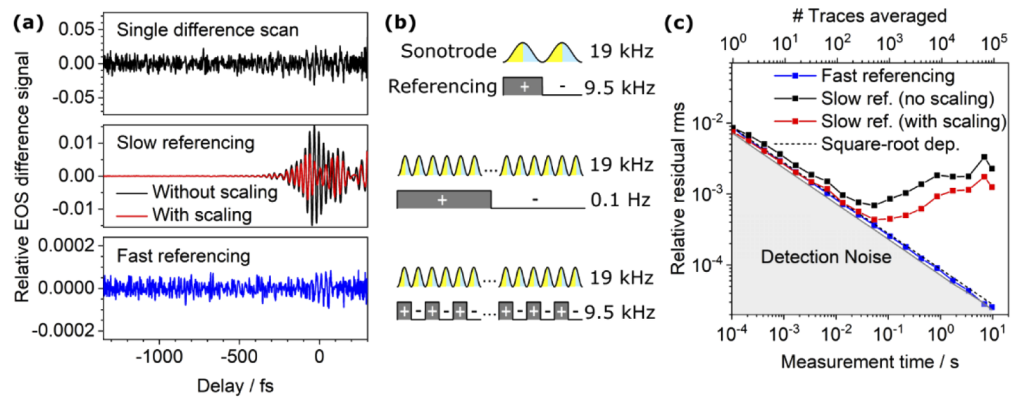


Fig. 4. Differential referencing of EOS traces. (a) Results of different referencing schemes. Top: difference between the averages of the traces acquired over two subsequent cycles of the sonotrode motion. Middle: averaging consecutive traces over 4.75 s before subtraction, without and with linear scaling of the second average trace to minimize the residual, mimicking “slow” referencing. Bottom: fast referencing, *i.e.*, averaging of the difference traces from subsequent cycles of the sonotrode motion (like in the top panel) for a total measurement time of 9.5 s. (b) Pictorial description of the referencing schemes. Yellow and blue shaded areas of the sonotrode oscillation indicate forward and backward motions respectively. The average of the traces indicated by the white areas of the referencing scheme is subtracted from the average of the traces indicated by the grey shaded areas. (c) Dependence of the relative RMS of the residual signal on measurement time for the cases shown in a, and comparison to the detection noise with a blocked mid-IR beam.

scan with a slowly moving stage low-frequency laser drifts distort the trace itself while it is being recorded, whereas in this case fast acquisition provides snap shots of the full waveform evolving over time. The residual structure of the difference trace (black) has a relative amplitude of ca. 2×10^{-2} and captures the slow waveform drifts already identified in the timing jitter analysis of Fig. 3. Two contributions to the difference signal can be distinguished: Changes of the signal amplitude with otherwise constant shape, from low-frequency laser intensity fluctuations (or beam pointing), and changes of the shape of the waveform itself, *e.g.*, from variation of the laser pulse spectrum. Scaling the second average trace before subtraction to minimize the residuum, removes the effect of trace-to-trace amplitude variation. The resulting red trace still evidences the slow drifts in waveform shape, which also appear in the timing jitter analysis.

Full advantage of fast acquisition is taken by averaging individual difference scans as the one in the top panel, for which referencing by subtraction is performed from one cycle to the next at 9.5 kHz (Fig. 4(a) and (b), bottom). With the same total acquisition time of 9.5 s as before, the signals now cancel almost completely except for a small residual structure around time zero. Not only is the appearance similar to that of the single difference scan, but also the RMS noise reduces with the square root of the number of averaged difference scans to 2.5×10^{-5} .

The dependence of the RMS noise of the difference signal on total measurement time is evaluated in Fig. 4(c). For the slow referencing of Fig. 4(a) and (b), middle, the RMS of the residuum decreases with measurement time only up to ca. 50 ms, beyond which it rises again due to the waveform drift also observed in the analysis of Fig. 3. Intensity correction by scaling slightly reduces the RMS. The noise then follows an initial square-root dependence with the number of traces averaged, indicating that the fast waveform distortions above 20 Hz are dominated by statistical noise. Performing the fast referencing of Fig. 4(a) and (b), bottom, extends the linear square-root dependence with the number of averaged traces up to our maximum measurement time of 9.5 s without any apparent deviation. The residual signal is close to the

detection noise with the blocked mid-IR beam (shaded gray) for all investigated measurement times. The statistical behavior of the residual RMS achieved by fast referencing allows to improve detection sensitivity by increasing the measurement time, with no limitation reached in the current experiment.

Ultra-rapid referencing by division in the frequency domain is explored in Fig. 5 (see appendix D for more details). In contrast to the differential referencing discussed above, in a spectroscopic measurement this operation ideally provides the device-independent pure sample response [35]. While pure intensity measurement techniques (*e.g.*, most Fourier-transform spectroscopies and direct absorption spectroscopy) yield absorption spectra only, EOS provides the full complex transfer function $H(\nu)$ of a sample, depending on frequency ν [1,36]:

$$H(\nu) = \frac{\mathcal{F}(S_S(\tau))}{\mathcal{F}(S_R(\tau))},$$

where $\mathcal{F}(S_S(\tau))$ and $\mathcal{F}(S_R(\tau))$ are the Fourier transforms of signal and reference EOS traces, recorded as a function of the delay τ . Moving to polar coordinates, Fig. 5 investigates the averaging behavior for $H(\nu)$ in terms of its magnitude $|H(\nu)|$ and phase $\phi = \arg(H(\nu))$, which are related to the imaginary and real parts of the refractive index, respectively [36].

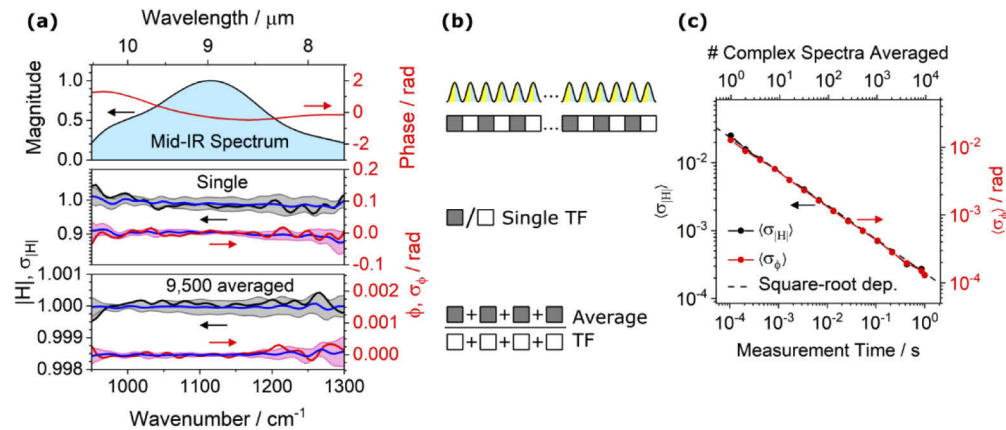


Fig. 5. Referencing by dividing the complex Fourier transform spectra of EOS traces. (a) Top: stationary normalized magnitude, and phase obtained from the complex Fourier transform of the pink average trace in Fig. 2(a). Below: magnitude and phase of the complex transfer function $H(\nu)$: single transfer functions from dividing the average complex spectra of two subsequent sonotrode cycles through each other, and average over 9,500 cycles (1 s of acquisition time) with fast referencing. Black/red: Magnitude and phase spectra, respectively; blue and shaded areas: mean and standard deviation of 9 TFs. (b) Pictorial description of TF calculation. (c) Dependence of the spectrally averaged standard deviations $\langle \sigma_{|H|} \rangle$ and $\langle \sigma_{\phi} \rangle$ on measurement time, and square-root dependent averaging behavior expected for averaging of data with statistical noise.

Figure 5(a) (top) shows the average magnitude spectrum of the mid-IR pulses together with the spectral phase. We limit our analysis to the spectral range 950-1300 cm^{-1} , where most of the mid-IR pulse energy is concentrated. As depicted in Fig. 5(b), the single complex transfer function (TF) with the magnitude and phase contributions in the middle panel of 5a (black and red, respectively) is obtained in analogy to Fig. 4 by summing the complex Fourier transform spectra in forward and backward direction for a single sonotrode oscillation cycle and dividing by the equivalent sum of the next cycle.

To investigate the statistics of averaging TFs, here we address the case of nominally identical sample and reference measurements, *i.e.*, the case of the identity TF. The *ab initio* expected

values for the magnitude and phase are 1 and 0, respectively. Residual oscillations are possibly a result of the interplay between noise and windowing on the Fourier transformation, as the EOS trace has still significant oscillation amplitude at the positive end of the delay range (*cf.* Figure 2(a)). Performing the arithmetic mean over 9 such TFs (blue, in Fig. 5(a), middle) reduces the spectral modulations. The shaded areas indicate the frequency-dependent standard deviations $\sigma_{|H|}(\nu)$ and $\sigma_{\phi}(\nu)$ around the mean. The unmodulated appearance of $\sigma_{|H|/\phi}(\nu)$ indicates that the spectral modulation of the TFs is statistical in nature. The spectral means of $\sigma_{|H|/\phi}(\nu)$ over the presented frequency range are $\langle\sigma_{|H|}\rangle = 2.5 \times 10^{-2}$ and $\langle\sigma_{\phi}\rangle = 1.3 \times 10^{-2}$ rad, respectively.

For averaging TFs with fast referencing, we add the traces of alternating cycles of the sonotrode before division (Fig. 5(b), bottom), instead of performing the arithmetic mean over the single TFs, in order to avoid artefacts from noise in the denominator. Performing this procedure over 9,500 sonotrode cycles, corresponding to 1 s of acquisition time, results in the black and red curves in Fig. 5(a), bottom. The appearance of the magnitude and phase curves resembles that for the single TFs. The standard deviation $\sigma_{|H|/\phi}(\nu)$ of 9 such magnitude and phase spectra (shaded areas) have again a smooth appearance around the arithmetic mean (blue), suggesting that the residual spectral modulation is mostly statistical in nature also at second-long measurement times. The spectral mean of $\sigma_{|H|/\phi}(\nu)$ has decreased for magnitude and phase to 2.2×10^{-4} and 1.3×10^{-4} rad, respectively, in agreement with a square-root dependence on the number of averages.

The dependence of the spectral mean of $\sigma_{|H|/\phi}(\nu)$ on the measurement time is studied in Fig. 5(c). Just as observed for the difference formation in Fig. 4(c), the noise of magnitude and phase of the transfer function reduces linearly with the square root of the number of contributing scans, and thus with measurement time. We conclude that the spectroscopic sensitivity strictly improves with increasing measurement time, with no limitation reached for our measurement times in the range of seconds.

4. Discussion

The unique combination of broad optical bandwidth, power scalability and attosecond-precision delay variation renders our sonotrode-based ultra-rapid EOS scan ideal both for tackling new applications that require high-speed acquisition, and for boosting the sensitivity of state-of-the-art field-resolved spectroscopy of static samples. Highly attractive prospects for the former include the observation of irreversible protein refolding in real time [12], and label-free cell fingerprinting in high-throughput [19].

On the other hand, our experiments show that the reduction of the acquisition time for single scans from several seconds to 26 μs (with a minimum of 8 gate pulses per mid-IR cycle) almost ‘freezes’ technical noise during single scans in a typical mid-IR field-resolving spectrometer. The square-root decrease of the standard deviation of referenced signals with the number of scans implies optimum averaging of the signals produced by single laser pulses, over acquisition times typical to static condensed-matter samples. This promises to significantly increase detection sensitivity in referenced spectroscopic measurements [3].

In our experiment, the time-domain electric-field DR of 150 for a single sonotrode-based EOS scan was mainly limited by the EOS conversion efficiency and the dynamic range of the 16-bit data acquisition card. In principle, the phase matching conditions and geometry of the intra-pulse difference-frequency generation and EOS can be optimized further to provide higher conversion efficiency and/or broader spectral bandwidth [3].

In the future, switching between sample and reference measurements at a frequency of 9.5 kHz can be readily achieved with conventional mechanical choppers. Promising applications include pump-probe type transient EOS measurements with a chopped pump beam, in which full waveforms are recorded for each pump-on and pump-off state, and ultra-sensitive mid-IR EOS measurements, in which a chopper alternates between sample and reference illumination.

The current delay range of 1.6 ps can be extended to several picoseconds by increasing the number of reflections at the sonotrode mirror. For Nyquist-limited EOS detection the maximum delay range τ_{\max} for any ultra-rapid scanning technique is reached, when the pulse-to-pulse delay equals half the period of the fastest oscillation to be resolved. For our spectral range and laser repetition rate $\tau_{\max} = 6.3$ ps holds, corresponding to a maximum spectral resolution of 5.3 cm^{-1} . For the delay calibration signal, which is generated with a continuous-wave laser, the Nyquist condition can always be met by choosing an appropriately fast data acquisition rate, with the only limitation given by the available data acquisition electronics.

The presented attosecond-precision delay calibration procedure reaches a reproducibility similar to that reported for acousto-optic based delay lines (15 as for single acquisitions at 34 kHz) [20]. Note that the latter approach uses the acoustic-to-optic translation to ensure intrinsic timing stability already in the delay generation process [37], whereas we achieve this timing precision by post-processing data recorded with a freely oscillating sonotrode. The presented delay calibration method is generally applicable beyond sonotrode scanning. The delay precision is mainly limited by the DR of the delay calibration signal, which could be further improved by using balanced detection. We also expect that implementing a true common interferometer for EOS and calibration beams by using a single beam combiner with an appropriately designed coating will improve the stability of the retrieved delay axis further. Note also that in contrast to other delay extraction techniques, we expect the predictor corrector algorithm to be applicable also to (partially) under-sampled calibration data beyond the Nyquist limit, as long as the timing jitter is smaller than half the oscillation period.

5. Conclusions

We presented an electro-optic sampling (EOS) setup for field-resolved mid-IR detection that uses an ultra-rapid sonotrode-based delay scanner to record full EOS traces of octave-spanning mid-IR pulses with 1.6-ps optical delay at a rate of 38 kHz. We traced the optical delay of the freely oscillating ultrasonic scanner interferometrically and employed a predictor corrector algorithm to extract the delay axis with down to single-digit attosecond precision, reproducible over hundreds of thousands of traces and several seconds of acquisition time. We showed for a single EOS trace a time-domain dynamic range of 150, corresponding to a spectral intensity dynamic range of 1.6×10^5 , which increases linearly with averaging time, reaching 4×10^{10} at an acquisition time of 9.5 s. We demonstrated two ultra-rapid referencing approaches, using difference formation and spectral division at 9.5 kHz that pave the way to increasing the sensitivity with measurement time also in sample/reference spectroscopic measurements, without reaching any limitations in our 9.5 s long acquisition. Referencing by spectral division provides the complex transfer function of the sample, for which we reached over the range 950-1300 cm^{-1} a spectroscopic sensitivity of 2.2×10^{-4} in magnitude and 0.13 mrad in spectral phase in an acquisition time of 1 s.

The presented technique for ultra-rapid EOS detection promises applications in the real-time measurement of irreversible chemical reactions, high-throughput flow cytometry and ultra-sensitive and highly reproducible field-resolved mid-IR molecular fingerprinting for disease detection. Furthermore, the sonotrode can in principle upgrade any linear or nonlinear optical experiment involving picosecond optical delays scans to acquisition with 38 kHz scan rate. The delay extraction algorithm we employed is also applicable to other ultra-rapid scanning techniques.

Appendix A: sonotrode mirror

Compared to a previous publication on sonotrode scanning [12], in which reflectivity was achieved by a gold coating directly on the sonotrode tip, we observed better optical quality, including less beam distortion, reduced scattering and losses, on attaching a gold mirror (20 mm diameter, 2 mm thickness) with epoxy glue to the sonotrode. Despite the immense acceleration

of the sonotrode mirror during the 60 μm (peak-to-peak) oscillation we did not observe any deterioration of the attachment over weeks of use.

Appendix B: delay predictor-corrector algorithm

Precise retrieval of the delay axis is a prerequisite in many linear and nonlinear experiments using a delay scanning technique. For example, precision field-resolved metrology harnessing the outstanding stability of optical waveforms obtained by intra-pulse difference-frequency generation requires the knowledge of the delay for each data point with sub-femtosecond precision [3,34]. Reliably tracking the instantaneous optical delay induced by the free mechanical oscillation of a mirror at > 10 kHz, with sub-femtosecond resolution, provides an additional challenge. For averaging traces in time domain not only the delay steps need to be determined precisely, but for acquisition times of seconds, hundreds of thousands of traces need to overlap in time.

In previous works, interferometrically encoded delay information was extracted by determining the positions of the zero transitions of the calibration signal [12], or by Fourier-transform techniques [28,38]. Here, we instead employed a progressing predictor-corrector algorithm. Compared to the zero-crossing approach the algorithm takes not only a few, but all acquired calibration data points into account. Another difference to the previous approaches is the use of the prior knowledge of the approximately sinusoidal oscillation of the sonotrode. Intrinsicly, a single interferogram is not sensitive to the direction of motion, so that any delay extraction with the aim of directly comparing and averaging time-domain traces needs to impose directionality as additional information. For our measurements we found much better long-term consistency of the absolute delay axes of the individual scans on using the sonotrode motion as the basis for the delay extraction algorithm in comparison with extracting the relative delays without employing prior knowledge to correct the delay axes during post-processing. Our algorithm also does not require phase unwrapping, which is typical for Fourier-domain approaches and can lead to ambiguities in the presence of noise. Another advantage of our algorithm, when compared, for example, to Fourier-transform based approaches, is the sequential processing from one data point to the next, making it compatible with real-time processing of a data stream from a measurement. The steps of the algorithm and its implementation are described below.

B.1. Data preparation

For convenience the interferometric oscillations of the calibration signal were normalized to the range $[-1, 1]$ by applying a segmental normalization with 170-point segment size (Fig. 6). Next, we identified the data indices n_{tp} corresponding to the turning points x of the sonotrode motion by the symmetry of the raw interferogram around these points (also shown in Fig. 6), *i.e.*, by finding the minimum

$$n_{tp} = \min_n \left[\sum_{i=1}^m (I_{raw}(n+i) - I_{raw}(n-i))^2 \right], \quad (1)$$

where n is the data index, I_{raw} is the intensity of the raw calibration signal, and m is the window size for symmetry evaluation (in our case 800). Note that data preprocessing can also be performed on a continuous data stream. The turning points are later used to cut the measured signal together with the extracted delays into individual forward and backward traces of the sonotrode cycle, and to estimate the cycle period of the sonotrode motion.

B.2. Description of the sonotrode motion and the calibration interferogram

For a mathematical treatment, we describe the optical delay τ as a cosine oscillation with data index n , defined by the oscillation period T (in number of data points) and the delay amplitude

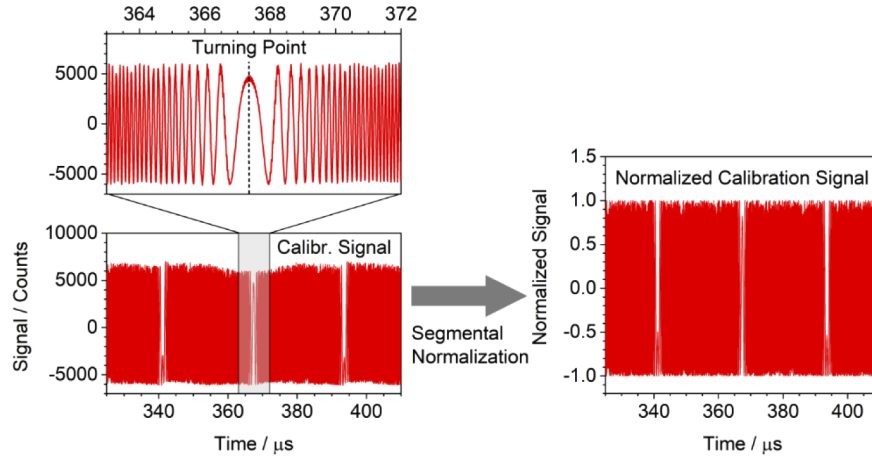


Fig. 6. Calibration data preprocessing. Left: raw calibration signal, and expanded section of the signal showing the mirror symmetry around a turning point of the sonotrode mirror. Segmental normalization prepares the calibration data for the delay extraction algorithm (right).

A_τ , corresponding to half the delay range of forward/backward movements:

$$\tau(n) = A_\tau \cos\left(\frac{2\pi}{T}(n - n_{tp0})\right) + \tau_0, \quad (2)$$

with the delay offset τ_0 , and n_{tp0} being the data index of the first turning point that corresponds to a delay maximum (to be determined from the directionality of the EOS signal traces). While the estimation of the sonotrode motion is not sufficiently precise to directly obtain the absolute delay axis, it allows to make a prediction for the relative delay step $\Delta\tau_{pred}(n)$ at data index n :

$$\begin{aligned} \Delta\tau_{pred}(n) &= \tau(n+1) - \tau(n) \approx \frac{d\tau}{dn} \Delta n \\ &= -A_\tau \frac{2\pi}{T} \sin\left(\frac{2\pi}{T}(n - n_{tp0} + 0.5)\right). \end{aligned} \quad (3)$$

The normalized interferometric signal oscillates with the sonotrode motion according to

$$I(n) = \sin\left(\frac{2\pi c}{\lambda}\tau(n) + \varphi\right), \quad (4)$$

where λ is the optical wavelength (here 1550 nm), and φ is the interferometric oscillation phase.

B.3. Initial conditions

The algorithm starts at the first turning point, n_{tp0} , with data index of the first turning point. For convenience, we set initially

$$\tau(n_{tp0}) = 0 \quad \text{and} \quad \tau_0 = -A_\tau. \quad (5)$$

The delay traces are later, during post-processing, shifted in time to coincide zero delay with the excitation pulse maximum. The initial estimate for the sonotrode period is given by the

difference of the data indices of the 1st and 3rd turning points:

$$T = n_{ip2} - n_{ip0} \quad (6)$$

The interferometric phase is given by

$$\varphi = \arcsin(I(n_{ip0})) - \frac{2\pi c}{\lambda} \tau(n_{ip0}) = \arcsin(I(n_{ip0})). \quad (7)$$

For an initial estimate, the delay amplitude A_τ can be obtained with other delay extraction methods. Here we deduced it from the number of zero crossings, a_{zc} , of the interferogram from one turning point to the next:

$$A_\tau = \frac{1}{4} a_{zc} \frac{\lambda}{c}. \quad (8)$$

B.4. Recursive predictor-corrector steps

The working principle of the recursive steps is depicted in Fig. 7. At each calibration data point with index n the expected next data point of the interferogram with index $(n + 1)$ is predicted, based on the current knowledge of the sonotrode motion. The deviation of the predicted and actual signals, ΔI , is then used to obtain a corrected solution for the sonotrode motion.

1. **Prediction.** Given the current delay $\tau(n)$ and the interferometric intensity $I(n)$ at acquisition index n , we use Eq. (3) to predict the delay step $\Delta\tau_{pred}(n)$. Employing Eq. (4) the predicted calibration signal intensity at data index $(n + 1)$ is then given by

$$I_{pred}(n + 1) = \sin\left(\frac{2\pi c}{\lambda} [\tau(n) + \Delta\tau_{pred}(n)] + \varphi\right). \quad (9)$$

2. **Correction.** Due to imperfect knowledge of the sonotrode motion, and due to experimental noise, the predicted value $I_{pred}(n + 1)$ and the actually measured value I_{n+1} deviate from each other by $\Delta I(n)$. To first approximation the actual delay step $\Delta\tau(n)$ can be obtained by a correction of the predicted delay step, $\Delta\tau_{pred}(n)$, according to

$$\Delta\tau(n) = \Delta\tau_{pred}(n) + \Delta I(n) \frac{\Delta\tau_{pred}(n)}{I_{pred}(n + 1) - I(n)}. \quad (10)$$

In order to improve convergence, we limited the delay step correction to a maximum of 5% of $\Delta\tau_{pred}(n)$. The new delay at index $(n + 1)$ is given by

$$\tau(n + 1) = \tau(n) + \Delta\tau(n). \quad (11)$$

3. **Redefinition of parameters** after completion of each sonotrode cycle. Every time the delay extraction completes a sonotrode cycle, *i.e.*, when the data index reaches the value of an even turning point, $n_{ip(2m+2)}$, with $m \in \mathbb{N}$, the parameters are redefined according to:

$$T = n_{ip(2m+2)} - n_{ip(2m)}, \quad (12)$$

$$A_\tau = \frac{1}{2} \left(\max_n(\tau(n)) - \min_n(\tau(n)) \right), \quad (13)$$

with $n \in \{n_{ip(2m)}, n_{ip(2m)} + 1, \dots, n_{ip(2m+2)}\}$.

4. Repetition of steps 1-3.

Figure 7(b) shows the delay extracted by the algorithm for the full data set (shifted such that zero delay coincides with the maximum of the EOS signal). The algorithm retrieved a delay axis that is consistent for all $> 10^9$ calibration data points (9.5 s acquisition time) and hundreds of thousands of delay scans, without producing any outliers, delay jumps or systematic drift. The zoom given by the inset reveals the oscillations of the extracted sonotrode delay.

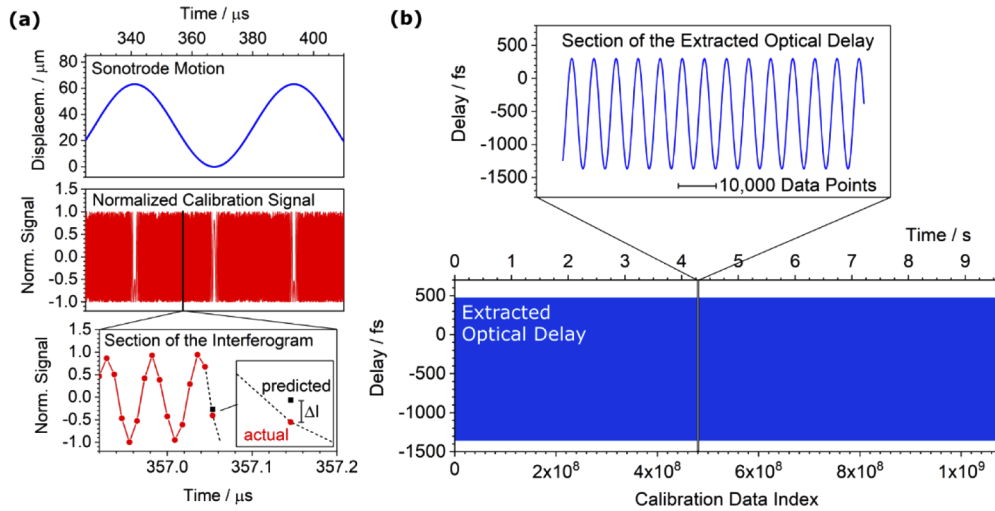


Fig. 7. Delay extraction algorithm and its performance. (a) Working principle of the algorithm. Starting from the calibration signal at data index n the algorithm predicts the signal value at data index $(n + 1)$. The difference between the predicted and actual signals at $(n + 1)$, ΔI , is used to correct the predicted sonotrode motion. (b) Optical delay extracted for the full data set (9.5 s acquisition time).

B.5. Post-processing

We applied the following post-processing steps:

1. **Low pass filtering of $\tau(n)$.** We applied a 2nd-order Butterworth low-pass filter with a cut-off frequency corresponding to 2.24 MHz (in data acquisition time) to the extracted delays $\tau(n)$. We assign delay variations above the cut-off frequency mainly to detection noise instead of actual sonotrode motion.
2. **Decimating signal and delay axes.** In the current experiment we recorded data at four times the laser repetition rate to ensure optimal sampling of the 1550-nm interference signal. Data was recorded without any intermittence, ensuring that strictly every 4th data point corresponds to a measurement with a laser shot. In this step we decimated the EOS signal and delay axis to only those measurement points, which coincide with a laser shot. The smoothing of the undecimated $\tau(n)$ by low-pass filtering in the last step also made sure that even after decimation the delay axis still carries average information of the discarded data points.
3. **Baseline correction of the EOS signal.** The baseline of the raw EOS signal carries modulation from slight pointing variation during the sonotrode movement. We performed a baseline correction by applying a 140 kHz high-pass filter, see Fig. 8(a).

4. **Separation into individual traces.** Using the turning points of the sonotrode motion, identified during data evaluation, we separated the continuous EOS signal and corresponding extracted delays $\tau(n)$ into individual forward and backward traces with the respective delay axes.
5. **Delay correction.** Because the Ge plate does not transmit 1550 nm light, the calibration and EOS beams do not share a fully common interferometer. In order to correct for the remaining drifts of the measured signals with respect to the extracted delay axes, we corrected each delay axis to reach optimum overlap of all EOS traces. For computational efficiency and convergence reasons we used here a linear fitting routine to extract the relative delay shift $\delta\tau_{i,fw}$ and $\delta\tau_{i,bw}$ of traces i in forward and backward directions. Let $S_{i,fw}(\tau)$ and $S_{i,bw}(\tau)$ be the i^{th} delay-dependent EOS traces for forward and backward scanning directions, respectively. We define a basis set consisting of two functions, B1(τ) and B2(τ), derived from the first EOS trace, $S_{0,fw}(\tau)$, according to

$$\begin{aligned} B1 &= S_{0,fw}(\tau), \\ B2 &= S_{0,fw}\left(\tau + \frac{1}{4\nu_c}\right). \end{aligned} \quad (14)$$

Where ν_c is the mid-IR carrier frequency (33.3 THz, in our case). B2 is therefore shifted by $\pi/2$ compared to B1, with respect to the carrier oscillation. Any traces $S_{i,fw}(\tau + \delta\tau_{i,fw})$ or $S_{i,bw}(\tau + \delta\tau_{i,bw})$ with small delay shift values $\delta\tau_{i,fw}$ and $\delta\tau_{i,bw}$ can be fitted by a linear combination of B1 and B2:

$$S_{i,fw/bw}(\tau + \delta\tau_{i,fw/bw}) = a_1 \times B1(\tau) + a_2 \times B2(\tau), \quad (15)$$

with the linear coefficients a_1 and a_2 . For the fitting procedure B1 and B2 were interpolated to the individual delay axes of $S_{i,fw}$ or $S_{i,bw}$ for each EOS trace. The delay shifts $\delta\tau_{i,fw}$ and $\delta\tau_{i,bw}$ were calculated from a_1 and a_2 using the atan2 function,

$$\delta\tau_{i,fw/bw} = \frac{1}{2\pi\nu_c} \text{atan2}(a_2, a_1). \quad (16)$$

The delay shifts $\delta\tau_{i,fw}$ and $\delta\tau_{i,bw}$, extracted for our 9.5-s long data set are shown in Fig. 8(c). Both forward and backward traces show only sub-femtosecond variations of the delay that are compatible with mechanical drift. Note that in the delay shift extraction not a single outlier is detected, confirming the consistency and reliability of the predictor-corrector algorithm. The slight, ca. 500 as, offset between forward and backward traces arises from a small temporal offset between the data acquisitions of signal and reference traces that can be easily corrected in future by adjusting the cable lengths or shifting the traces relative to each other during post processing.

Each individual trace was corrected for the respective delay shift $\delta\tau_{i,fw}$ or $\delta\tau_{i,bw}$. For all traces the same basis set functions B1 and B2 were used for fitting, so that any delay shifts including the offset between forward and backward scans were intrinsically corrected.

6. **Interpolation to a common delay axis.** We interpolated all EOS forward and backward traces to a common delay axis (delay axis of $S_{0,fw}$), using spline interpolation.

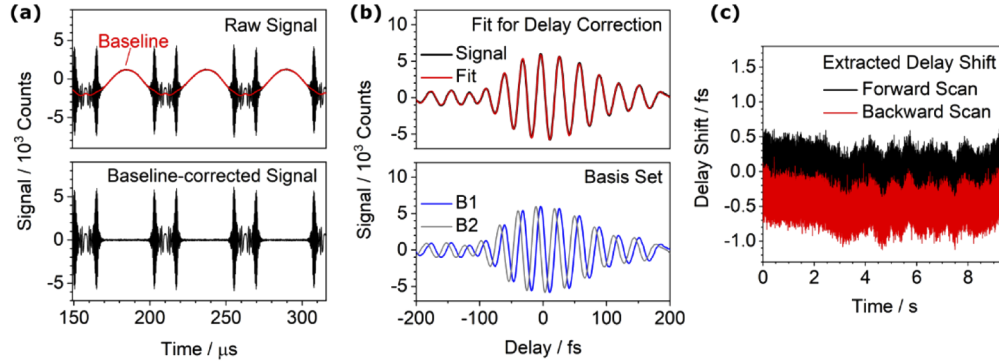


Fig. 8. Data post processing. (a) The EOS raw data was baseline corrected by applying a Fourier high-pass filter. (b) For delay correction each EOS trace is fitted by a linear combination of two traces, B1 and B2, which are shifted by $\pi/2$ of the mid-IR carrier oscillation. (c) Delay shifts $\delta\tau_{i,fw}$ and $\delta\tau_{i,bw}$, extracted from the fit depicted in (b).

Appendix C: differential referencing

In the previous notation we define the single difference scan by

$$\Delta S_j(\tau) = \frac{S_{fw,2j}(\tau) + S_{bw,2j}(\tau)}{2} - \frac{S_{fw,2j+1}(\tau) + S_{bw,2j+1}(\tau)}{2}, \quad \text{with } j \in \mathbb{N}, \quad (17)$$

For slow referencing (Fig. 4(a), middle), the difference signal for an averaging number n is given by

$$\langle \Delta S(\tau) \rangle_{slow} = \frac{1}{2n} \sum_{i=0}^{n-1} (S_{i,fw}(\tau) + S_{i,bw}(\tau)) - \frac{1}{2n} \sum_{i=n}^{2n-1} (S_{i,fw}(\tau) + S_{i,bw}(\tau)) \quad (18)$$

For fast referencing the average difference signal is defined by

$$\langle \Delta S(\tau) \rangle_{fast} = \frac{1}{n} \sum_{j=0}^{n-1} \Delta S_j(\tau). \quad (19)$$

Appendix D: spectral referencing

In a linear spectroscopic experiment, the recorded EOS traces in time domain, $S(\tau)$, can be described by the convolution of electric field $E(\tau)$ of the mid-IR excitation pulse with the instrument response function $R(\tau)$ and the temporal response $H(\tau)$ of the sample,

$$S(\tau) = E(\tau) \otimes R(\tau) \otimes H(\tau) \quad (20)$$

Upon Fourier transformation the equation becomes:

$$\mathcal{F}(S(\tau)) = E(\nu) \times R(\nu) \times H(\nu), \quad (21)$$

where $E(\nu)$ is the complex electric field of the mid-IR pulse in frequency domain, $R(\nu)$ is the complex instrument transfer function, and $H(\nu)$ is the complex transfer function (TF) of the induced sample change. Dividing the complex Fourier transforms of sample and reference traces

from a spectroscopic experiment (S_S and S_R , respectively) thus reveals the pure sample transfer function $H(\nu)$:

$$H(\nu) = \frac{\mathcal{F}(S_S(\tau))}{\mathcal{F}(S_R(\tau))}. \quad (22)$$

The single transfer function $H_j(\nu)$ in Fig. 5(a) was obtained by summing the complex Fourier transform spectra in forward and backward directions for the single sonotrode oscillation cycle j and dividing through the equivalent sum of the next cycle ($j+1$), *i.e.*,

$$H_j(\nu) = \frac{\mathcal{F}(S_{j,fw}(\tau)) + \mathcal{F}(S_{j,bw}(\tau))}{\mathcal{F}(S_{j+1,fw}(\tau)) + \mathcal{F}(S_{j+1,bw}(\tau))}. \quad (23)$$

The average transfer functions in Fig. 5(a), bottom, is defined by

$$\langle H(\nu) \rangle = \frac{\sum_{j=0}^{n-1} [\mathcal{F}(S_{2j,fw}(\tau)) + \mathcal{F}(S_{2j,bw}(\tau))]}{\sum_{j=0}^{n-1} [\mathcal{F}(S_{2j+1,fw}(\tau)) + \mathcal{F}(S_{2j+1,bw}(\tau))]} . \quad (24)$$

The standard deviation of magnitude and phase, $\sigma_{|H|}(\nu)$ and $\sigma_{\phi}(\nu)$, were calculated over nine consecutive single or average TFs. The spectrally averaged standard deviations for magnitude and phase TFs are given by

$$\langle \sigma_{|H|/\phi} \rangle = \frac{1}{\nu_2 - \nu_1} \int_{\nu_1}^{\nu_2} \sigma_{|H|/\phi}(\nu) \, d\nu. \quad (25)$$

The values $\langle \sigma_{|H|} \rangle$ and $\langle \sigma_{\phi} \rangle$ in Fig. 5(c) are the mean of all independent spectrally averaged standard deviations that can be obtained from the full data set for a given number of complex spectra averaged.

Disclosures. The authors declare no conflicts of interest.

Data availability. Data underlying the results presented in this paper are not publicly available at this time but may be obtained from the authors upon reasonable request.

References

- G. Gallot and D. Grischkowsky, "Electro-optic detection of terahertz radiation," *J. Opt. Soc. Am. B* **16**(8), 1204–1212 (1999).
- A. S. Kowligy, H. Timmers, A. J. Lind, U. Elu, F. C. Cruz, P. G. Schunemann, J. Biegert, and S. A. Diddams, "Infrared electric field sampled frequency comb spectroscopy," *Sci. Adv.* **5**(6), eaaw8794 (2019).
- I. Pupeza, M. Huber, M. Trubetskov, W. Schweinberger, S. A. Hussain, C. Hofer, K. Fritsch, M. Poetzlberger, L. Vamos, E. Fill, T. Amotchkina, K. V. Kepesidis, A. Apolonski, N. Karpowicz, V. Pervak, O. Pronin, F. Fleischmann, A. Azzeer, M. Žigman, and F. Krausz, "Field-resolved infrared spectroscopy of biological systems," *Nature* **577**(7788), 52–59 (2020).
- S. Keiber, S. Sederberg, A. Schwarz, M. Trubetskov, V. Pervak, F. Krausz, and N. Karpowicz, "Electro-optic sampling of near-infrared waveforms," *Nat. Photonics* **10**(3), 159–162 (2016).
- P. U. Jepsen, D. G. Cooke, and M. Koch, "Terahertz spectroscopy and imaging – Modern techniques and applications," *Laser Photonics Rev.* **5**(1), 124–166 (2011).
- M. Huber, M. Trubetskov, S. A. Hussain, W. Schweinberger, C. Hofer, and I. Pupeza, "Optimum sample thickness for trace analyte detection with field-resolved infrared spectroscopy," *Anal. Chem.* **92**(11), 7508–7514 (2020).
- P. R. Griffiths and J. A. de Haseth, *Fourier Transform Infrared Spectrometry* (Wiley, 2007).
- M. Maiuri, M. Garavelli, and G. Cerullo, "Ultrafast spectroscopy: state of the art and open challenges," *J. Am. Chem. Soc.* **142**(1), 3–15 (2020).
- M. Huber, W. Schweinberger, F. Stutzki, J. Limpert, I. Pupeza, and O. Pronin, "Active intensity noise suppression for a broadband mid-infrared laser source," *Opt. Express* **25**(19), 22499–22509 (2017).
- C. Riek, D. V. Seletskiy, A. S. Moskalenko, J. F. Schmidt, P. Krauspe, S. Eckart, S. Eggert, G. Burkard, and A. Leitenstorfer, "Direct sampling of electric-field vacuum fluctuations," *Science* **350**(6259), 420–423 (2015).

11. M. Porer, J.-M. Ménard, and R. Huber, "Shot noise reduced terahertz detection via spectrally postfiltered electro-optic sampling," *Opt. Lett.* **39**(8), 2435–2438 (2014).
12. B. Süß, F. Ringleb, and J. Heberle, "New ultrarapid-scanning interferometer for FT-IR spectroscopy with microsecond time-resolution," *Rev. Sci. Instrum.* **87**(6), 063113 (2016).
13. E. Ritter, L. Puskar, S. Y. Kim, J. H. Park, K. P. Hofmann, F. Bartl, P. Hegemann, and U. Schade, "Féry infrared spectrometer for single-shot analysis of protein dynamics," *J. Phys. Chem. Lett.* **10**(24), 7672–7677 (2019).
14. P. R. Griffiths, B. L. Hirsche, and C. J. Manning, "Ultra-rapid-scanning Fourier transform infrared spectrometry," *Vib. Spectrosc.* **19**(1), 165–176 (1999).
15. K. Hashimoto, M. Takahashi, T. Ideguchi, and K. Goda, "Broadband coherent Raman spectroscopy running at 24,000 spectra per second," *Sci. Rep.* **6**(1), 21036 (2016).
16. I. Radu, M. Schleegeer, C. Bolwien, and J. Heberle, "Time-resolved methods in biophysics. 10. Time-resolved FT-IR difference spectroscopy and the application to membrane proteins," *Photochem. Photobiol. Sci.* **8**(11), 1517–1528 (2009).
17. C.-S. Liao, K.-C. Huang, W. Hong, A. J. Chen, C. Karanja, P. Wang, G. Eakins, and J.-X. Cheng, "Stimulated Raman spectroscopic imaging by microsecond delay-line tuning," *Optica* **3**(12), 1377–1380 (2016).
18. M. S. Alshaykh, C.-S. Liao, O. E. Sandoval, G. Gitzinger, N. Forget, D. E. Leaird, J.-X. Cheng, and A. M. Weiner, "High-speed stimulated hyperspectral Raman imaging using rapid acousto-optic delay lines," *Opt. Lett.* **42**(8), 1548–1551 (2017).
19. K. Hiramatsu, T. Ideguchi, Y. Yonamine, S. Lee, Y. Luo, K. Hashimoto, T. Ito, M. Hase, J.-W. Park, Y. Kasai, S. Sakuma, T. Hayakawa, F. Arai, Y. Hoshino, and K. Goda, "High-throughput label-free molecular fingerprinting flow cytometry," *Sci. Adv.* **5**(1), eaau0241 (2019).
20. O. Schubert, M. Eisele, V. Crozatier, N. Forget, D. Kaplan, and R. Huber, "Rapid-scan acousto-optical delay line with 34 kHz scan rate and 15 as precision," *Opt. Lett.* **38**(15), 2907–2910 (2013).
21. B. Urbanek, M. Möller, M. Eisele, S. Baierl, D. Kaplan, C. Lange, and R. Huber, "Femtosecond terahertz time-domain spectroscopy at 36 kHz scan rate using an acousto-optic delay," *Appl. Phys. Lett.* **108**(12), 121101 (2016).
22. S. Kray, F. Spöler, T. Hellerer, and H. Kurz, "Electronically controlled coherent linear optical sampling for optical coherence tomography," *Opt. Express* **18**(10), 9976–9990 (2010).
23. Y. Kim and D.-S. Yee, "High-speed terahertz time-domain spectroscopy based on electronically controlled optical sampling," *Opt. Lett.* **35**(22), 3715–3717 (2010).
24. M. Kolano, O. Boidol, D. Molter, and G. V. Freymann, "Single-laser, polarization-controlled optical sampling system," *Opt. Express* **26**(23), 30338–30346 (2018).
25. O. Kliebisch, D. C. Heinecke, and T. Dekorsy, "Ultrafast time-domain spectroscopy system using 10 GHz asynchronous optical sampling with 100 kHz scan rate," *Opt. Express* **24**(26), 29930–29940 (2016).
26. R. J. B. Dietz, N. Vieweg, T. Puppe, A. Zach, B. Globisch, T. Göbel, P. Leisching, and M. Schell, "All fiber-coupled THz-TDS system with kHz measurement rate based on electronically controlled optical sampling," *Opt. Lett.* **39**(22), 6482–6485 (2014).
27. N. G. Chen and Q. Zhu, "Rotary mirror array for high-speed optical coherence tomography," *Opt. Lett.* **27**(8), 607–609 (2002).
28. K. Hashimoto and T. Ideguchi, "Phase-controlled Fourier-transform spectroscopy," *Nat. Commun.* **9**(1), 4448 (2018).
29. J. Brons, V. Pervak, D. Bauer, D. Sutter, O. Pronin, and F. Krausz, "Powerful 100-fs-scale Kerr-lens mode-locked thin-disk oscillator," *Opt. Lett.* **41**(15), 3567–3570 (2016).
30. K. Fritsch, M. Poetzlberger, V. Pervak, J. Brons, and O. Pronin, "All-solid-state multipass spectral broadening to sub-20 fs," *Opt. Lett.* **43**(19), 4643–4646 (2018).
31. I. Pupeza, D. Sánchez, J. Zhang, N. Lilienfein, M. Seidel, N. Karpowicz, T. Paasch-Colberg, I. Znakovskaya, M. Pescher, W. Schweinberger, V. Pervak, E. Fill, O. Pronin, Z. Wei, F. Krausz, A. Apolonski, and J. Biegert, "High-power sub-two-cycle mid-infrared pulses at 100 MHz repetition rate," *Nat. Photonics* **9**(11), 721–724 (2015).
32. Q. Wu and X. C. Zhang, "Free-space electro-optic sampling of terahertz beams," *Appl. Phys. Lett.* **67**(24), 3523–3525 (1995).
33. A. Baltuška, T. Fuji, and T. Kobayashi, "Controlling the carrier-envelope phase of ultrashort light pulses with optical parametric amplifiers," *Phys. Rev. Lett.* **88**(13), 133901 (2002).
34. S. A. Hussain, W. Schweinberger, T. Buberl, C. Hofer, and I. Pupeza, "Train of ultrashort mid-infrared pulses with sub-mrad carrier-envelope phase stability," in *CLEO/Europe-QECC* (Munich, Germany, 2019).
35. W. Demtröder, *Laser spectroscopy - basic concepts and instrumentation* (Springer, 1996).
36. I. Pupeza, R. Wilk, and M. Koch, "Highly accurate optical material parameter determination with THz time-domain spectroscopy," *Opt. Express* **15**(7), 4335–4350 (2007).
37. P. Tournois, "Acousto-optic programmable dispersive filter for adaptive compensation of group delay time dispersion in laser systems," *Opt. Commun.* **140**(4-6), 245–249 (1997).
38. P. Giaccari, J.-D. Deschênes, P. Saucier, J. Genest, and P. Tremblay, "Active Fourier-transform spectroscopy combining the direct RF beating of two fiber-based mode-locked lasers with a novel referencing method," *Opt. Express* **16**(6), 4347–4365 (2008).